



HAL
open science

A Lyman limit system associated with galactic winds

Hadi Rahmani, Céline Péroux, Ilane Schroetter, Ramona Augustin, Nicolas Bouché, Jens-Kristian Krogager, Varsha P. Kulkarni, Bruno Milliard, Palle Møller, Max Pettini, et al.

► **To cite this version:**

Hadi Rahmani, Céline Péroux, Ilane Schroetter, Ramona Augustin, Nicolas Bouché, et al.. A Lyman limit system associated with galactic winds. *Monthly Notices of the Royal Astronomical Society*, 2018, 480 (4), pp.5046-5059. 10.1093/mnras/sty2216 . hal-01871629

HAL Id: hal-01871629

<https://hal.science/hal-01871629>

Submitted on 3 May 2023

HAL is a multi-disciplinary open access archive for the deposit and dissemination of scientific research documents, whether they are published or not. The documents may come from teaching and research institutions in France or abroad, or from public or private research centers.

L'archive ouverte pluridisciplinaire **HAL**, est destinée au dépôt et à la diffusion de documents scientifiques de niveau recherche, publiés ou non, émanant des établissements d'enseignement et de recherche français ou étrangers, des laboratoires publics ou privés.

A Lyman limit system associated with galactic winds[★]

Hadi Rahmani,^{1,2†} Céline Péroux,² Ilane Schroetter,¹ Ramona Augustin,^{2,3}
Nicolas Bouché,⁴ Jens-Kristian Krogager,⁵ Varsha P. Kulkarni,⁶ Bruno Milliard,²
Palle Møller,³ Max Pettini,⁷ Joël Vernet³ and Donald G. York^{8,9}

¹GEPI, Observatoire de Paris, PSL Université, CNRS, 5 Place Jules Janssen, F-92190 Meudon, France

²LAM (Laboratoire d'Astrophysique de Marseille), Aix Marseille Université, CNRS, UMR 7326, F-13388 Marseille, France

³European Southern Observatory, Karl-Schwarzschildstrasse 2, D-85748 Garching bei München, Germany

⁴CNRS/IRAP, 9 Avenue Colonel Roche, F-31400 Toulouse, France

⁵Institut d'Astrophysique de Paris, CNRS-UPMC, UMR7095, 98bis bd Arago, F-75014 Paris, France

⁶Department of Physics and Astronomy, University of South Carolina, Columbia, SC 29208, USA

⁷Institute of Astronomy, University of Cambridge, Madingley Road, Cambridge CB3 0HA, UK

⁸Department of Astronomy and Astrophysics, The University of Chicago, Chicago, IL 60637, USA

⁹Enrico Fermi Institute, The University of Chicago, Chicago, IL 60637, USA

Accepted 2018 August 10. Received 2018 July 19; in original form 2018 March 22

ABSTRACT

Projected quasar galaxy pairs provide powerful means to study the circumgalactic medium (CGM) that maintains the relics of galactic feedback and the accreted gas from the intergalactic medium. Here, we study the nature of a Lyman Limit system (LLS) with $N(\text{H I}) = 10^{19.1 \pm 0.3} \text{ cm}^{-2}$ and a dust-uncorrected metallicity of $[\text{Fe}/\text{H}] = -1.1 \pm 0.3$ at $z = 0.78$ towards Q0152 – 020. The Mg II absorption profiles are composed of a main saturated and a few weaker optically thin components. Using MUSE observations, we detect one galaxy close to the absorption redshift at an impact parameter of 54 kpc. This galaxy exhibits nebular emission lines from which we measure a dust-corrected star formation rate of $10_{-5}^{+8} M_{\odot} \text{ yr}^{-1}$ and an emission metallicity of $[\text{O}/\text{H}] = -0.1 \pm 0.2$. By combining the absorption line kinematics with the host galaxy morphokinematics we find that while the main absorption component can originate from a galactic wind at $V_w = 110 \pm 4 \text{ km s}^{-1}$ the weaker components cannot. We estimate a mass ejection rate of $\dot{M} \gtrsim 0.8 M_{\odot} \text{ yr}^{-1}$ that translates to a loading factor of $\eta \gtrsim 0.1$. Since the local escape velocity of the halo, $V_{\text{esc}} \simeq 430 \text{ km s}^{-1}$, is a few times larger than V_w , we expect this gas will remain bound to the host galaxy. These observations provide additional constraints on the physical properties of winds predicted by galaxy formation models. We also present the VLT/X-Shooter data analysis of four other absorbing systems at $1.1 < z < 1.5$ in this sightline with their host galaxies identified in the MUSE data.

Key words: galaxies: abundances – galaxies: ISM – galaxies: kinematics and dynamics – quasars: absorption lines – quasars: individual: Q0152 – 020.

1 INTRODUCTION

The circumgalactic medium (CGM) is the region around a galaxy through which the baryon exchange between the intergalactic medium (IGM) and the galaxy occurs. On the one hand, it hosts the fresh pristine gas entering the halo from the IGM, but on the other hand, it contains relics of metal-enriched galactic winds. While

the extent of the CGM varies based on the definition, usually it is considered as the region with a radius of ~ 300 kpc surrounding galaxies (e.g. Steidel et al. 2010; Shull 2014). To understand the full cycle of gas from IGM into galaxies and from galaxies towards IGM it is crucial to understand the distribution, kinematics, and metal content of the gas in the CGM.

Due to the very low density of the gas, it is not yet possible to probe the CGM in emission (but see, Frank et al. 2012). Absorption lines towards background quasars provide the most sensitive tools to carry out CGM studies. In particular, quasar absorbers with large HI column density, $N(\text{H I}) \gtrsim 10^{19} \text{ cm}^{-2}$, afford robust measurements of the metal content of the CGM. There are several studies that also show that the majority of the neutral gas reservoirs in the Universe

[★]Based on data obtained under the ESO programmes 096.A-0303 and 095.A-0338 at the European Southern Observatories with MUSE at the 8.2 m telescopes operated at the Paranal Observatory, Chile.

†E-mail: hadi.rahmani@gmail.com

are associated with such absorbers (Péroux et al. 2003; Prochaska, Herbert-Fort & Wolfe 2005; Noterdaeme et al. 2009, 2012b; Zafar et al. 2013). Therefore, by studying such strong H I absorbers one not only probes the CGM but also traces the possible fuel for forming stars in galaxies.

Quiret et al. (2016) reported a bimodal distribution of metallicity for a subsample of strong H I absorbers ($19.0 < \log [N(H\text{I})/\text{cm}^{-2}] < 20.3$) at $z < 1$. The high-metallicity side of the distribution could be interpreted as a possible tracer for galactic winds and the low-metallicity side as a possible tracer for the pristine IGM gas accretion (see also Lehner et al. 2013; Wotta et al. 2016, for similar results but for Lyman limit systems (LLS) with $N(\text{H I}) > 10^{16} \text{ cm}^{-2}$). Hafen et al. (2016) studied a sample of LLS at similar redshifts extracted from hydrodynamical simulations where they demonstrated that such absorbers are associated with gaseous complexes in the CGM. While their mean LLS metallicity ($[X/H] = -0.9$) is consistent with that of observations, they did not find a bimodal metallicity distribution. It is worth also noting that in their simulation, Hafen et al. (2016) did not find as many low-metallicity systems as those detected in observations. However, to disentangle the role of the CGM gas, one needs to study together the LLS and its host galaxy.

The CGM can also be studied from the metal absorption lines in the spectra of the host galaxies themselves, the so-called down-the-barrel technique (e.g. Pettini et al. 2002; Steidel et al. 2010; Martin et al. 2012; Rubin et al. 2012; Kacprzak et al. 2014; Erb 2015; Bordoloi et al. 2016; Finley et al. 2017). Blueshifted and redshifted absorption lines are produced in the spectra of galaxies in the cases of, respectively, galactic winds and infalling gas. Large sample studies have been successful in finding predominantly outflows; infalling gas has been unambiguously identified in only a few cases (Martin et al. 2012; Rubin et al. 2012). Rubin et al. (2012) postulated that the strong and broad absorption lines from outflowing gas can smear out the absorption signature from infalling gas. In any case, the low-resolution spectra of galaxies and the unknown distance between absorbing gas and the host galaxy limit the ultimate accuracy of the derived physical parameters from down-the-barrel studies.

The nature of the gas in the CGM can be studied in more detail when the host galaxies of quasar absorbers are also detected in emission (Møller & Warren 1998; Rahmani et al. 2010; Péroux et al. 2011a,b; Noterdaeme et al. 2012a; Bouché et al. 2013; Christensen et al. 2014; Rahmani et al. 2016, 2018; Møller et al. 2017). As an example, Noterdaeme et al. (2012a) studied multiple emission lines from the host galaxy of a strong H I absorber at $z = 2.2$ and demonstrated that the absorption is most likely associated with an outflow (see also, Kulkarni et al. 2012). Krogager et al. (2012) observed a tight anti-correlation between the impact parameter and the $N(\text{H I})$ which is likely driven by feedback mechanisms (see also Monier, Turnshek & Rao 2009; Rao et al. 2011; Rahmani et al. 2016, for similar results).

Much better understanding on the nature of the CGM can be achieved if one combines the absorption line kinematics with those of the host galaxy absorber extracted from integral field unit (IFU) observation. As part of the SIMPLE survey (Bouché et al. 2007, 2012), in a study of the host galaxies of strong Mg II absorbers, Schroetter et al. (2015) demonstrated that such absorbers are often associated with galactic winds. Péroux et al. (2011a) used VLT/SINFONI IFU observations of the field of a handful of Damped Lyman- α systems (that are absorbers having $\log [N(H\text{I})/\text{cm}^{-2}] > 20.3$) at $z \sim 1$ to study the kinematics of their host galaxies. They also showed that the detection rate is higher for

the subsample of absorbers with higher metallicity. Rahmani et al. (2018) used VLT/MUSE observation of an LLS host galaxy along with high-resolution Keck/HIRES data of the quasar absorption line to show that the LLS originates from a warped disc. Such warped discs are probably associated with cold gas accreting onto galaxies (see also Bouché et al. 2013; Burchett et al. 2013; Diamond-Stanic et al. 2016, for similar studies).

Here, we present the detailed study of an LLS at $z = 0.78$ towards Q0152 – 020¹ (Sargent, Steidel & Boksenberg 1988b; Rao, Turnshek & Nestor 2006). We combine new VLT/MUSE observation of the quasar field with high spectral resolution Keck/HIRES, low spectral resolution HST/FOS spectroscopy of the quasar and HST/WFPC2 F702W high spatial resolution image to understand the nature of the CGM gas absorber. The paper is organized as follows. In Section 2, we provide a summary of the available observations. In Section 3, we study the absorption line, and in Section 4, we present the properties of the host galaxy absorber. In Section 5, we study the nature of the gas we see in absorption, and finally, we summarize the paper in Section 6. We also mention other absorbing systems in this sightline having redshifts $1.0 < z < 1.5$ in appendices B and C. Throughout this paper, we assume a flat Λ CDM cosmology with $H_0 = 69.3 \text{ km s}^{-1} \text{ Mpc}^{-1}$ and $\Omega_m = 0.286$ (Hinshaw et al. 2013).

2 OBSERVATIONS OF THE FIELD OF Q0152–020

In this section we summarize the spectroscopic and imaging observations of the field of Q0152–020. Apart from VLT/X-Shooter observations, the remaining data have been discussed in detail by Rahmani et al. (2018). Hence, while we present the X-Shooter observations in Appendix A, we only summarize the rest of the data and refer the reader to Rahmani et al. (2018) for a comprehensive description.

A field of view of $\sim 2 \text{ arcmin}^2$ around this quasar has been observed with *Hubble Space Telescope* Wide-Field Planetary Camera 2 (HST/WFPC2) F702W with a $0.1''$ pixel scale and resolution $FWHM = 0.2''$ (PI: Steidel, Program ID: 6557). The available Keck/HIRES spectrum of this quasar (O’Meara et al. 2015) covers a wavelength range of 3245 \AA to 5995 \AA and has a spectral resolution of $R = 48000$. IFU data of Q0152–020 has been obtained from VLT/MUSE observations (program 96.A-0303, PI: Péroux) with 100-min exposure time. We refer the reader to Péroux et al. (2017) for a complete description of the procedure used to reduce these VLT/MUSE data. The VLT/MUSE data have a spectral resolution of 2.6 \AA with a sampling of $1.25 \text{ \AA}/\text{pixel}$ and a wavelength coverage of 4750 \AA – 9350 \AA . Our final reduced cube has its wavelength scale in air and hence to obtain the redshifts we use the rest-frame wavelengths of nebular transitions as measured in air. The results remain the same if we convert the wavelength scale of the cube into vacuum and utilize the rest-frame wavelengths in vacuum.

It has been demonstrated that the light distribution of point sources in VLT/MUSE can be well described by a Moffat function (Bacon et al. 2015; Contini et al. 2016). To obtain the seeing of the MUSE final combined data, we generated narrow-band images of the quasar over several wavelength ranges and modelled them using GALFIT (Peng et al. 2010). As a typical value, we found an $FWHM = 0.6''$ ($\equiv 2.95 \text{ pixel}$) at $\lambda \sim 6640 \text{ \AA}$. We neglected the

¹RA(J2000) = 28.113464, Dec(J2000) = -20.018435 .

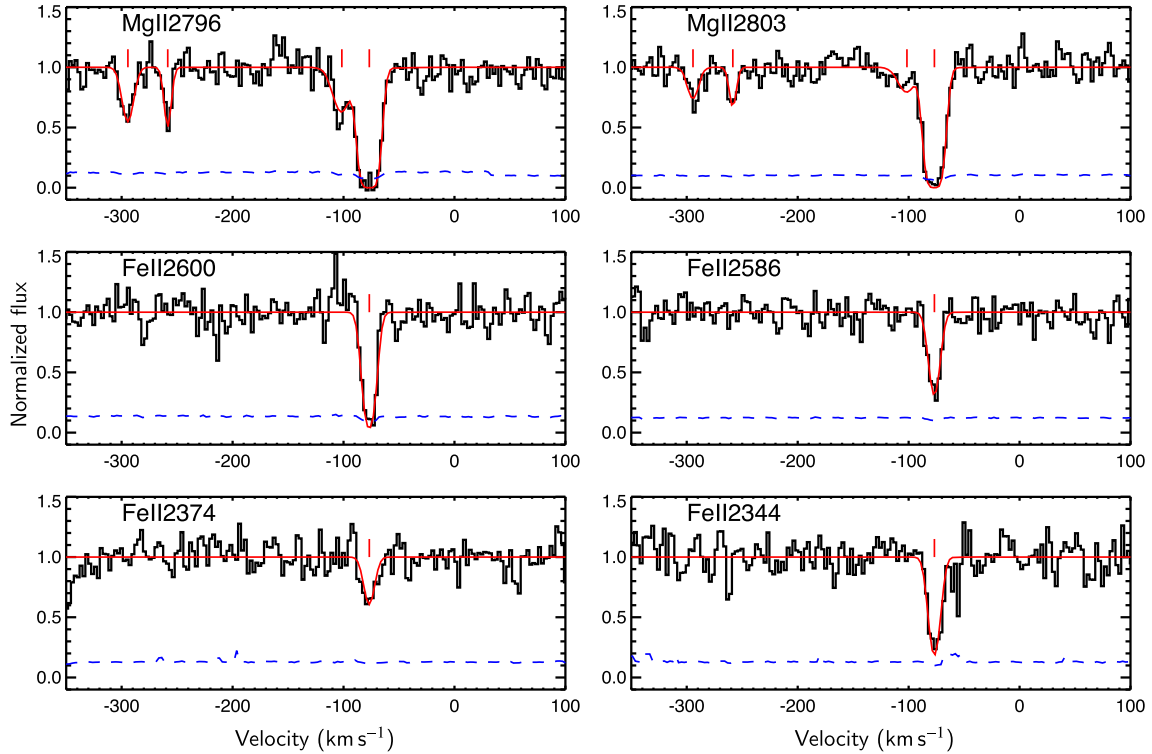


Figure 1. Normalized Keck/HIRES quasar absorption line spectrum. The zero velocity is set at the systemic redshift of the detected galaxy, $z = 0.78025$. Black histogram and red continuous lines represent the observed and modelled spectra, respectively. The blue dashed lines show the one sigma photon noise at each datapoint. The positions of Voigt profile components are indicated using vertical tick marks.

spatial variations of the FWHM over the MUSE field of view as it has been shown to be only a few per cent (Contini et al. 2016).

To extract the spectra of different objects from the MUSE cube, we use the MUSE PYTHON Data Analysis Framework (MPDAF v2.0) which is a Python-based package, developed by the MUSE Consortium (Piqueras et al. 2017).

3 QUASAR ABSORPTION LINE SYSTEMS

There are several intervening absorption line systems in the sightline of this quasar which is at emission redshift $z_{em} = 2.139$ (Sargent, Boksenberg & Steidel 1988a). The combination of the Keck/HIRES and X-Shooter spectra provides us with powerful means to study these absorbers. The two absorbing systems at $z = 0.38$ and $z = 0.78$ were already known from previous studies of this sightline (Sargent et al. 1988b; Guillemin & Bergeron 1997; Ellison, Kewley & Mallén-Ornelas 2005; Rao et al. 2006; Kacprzak et al. 2007; Rahmani et al. 2018). While we find absorber systems over the redshift range from $z = 0.38$ to $z = 2.13$, we limit this study to those at $z < 1.5$ as at larger redshifts the [O II] $\lambda\lambda 3727, 3729$ (or simply [O II]) in the remaining of the paper) emission line falls out of the MUSE wavelength coverage.

To model the absorption lines, we use the Voigt profile fitting code VPFIT² v10.0. In our Voigt profile model, we assume a given component to have the same redshift and broadening parameter for all transitions. We relax this constraint when we model C IV absorption profiles. The gas associated with C IV absorption lines

may not be co-spatial with that of singly ionized species. The X-Shooter and Keck/HIRES data are in vacuum and hence to obtain the redshifts and velocities we use the vacuum rest frame wavelengths of different transitions.

In the following, we present the absorption line analysis of the absorbing system at $z = 0.78$. Analysis of the remaining systems in this sightline is summarized in Appendix B. We also exclude the system at $z = 0.38$ from the following as the detailed study of this system was reported in our recent work (Rahmani et al. 2018).

3.1 The LLS system at $z_{abs} = 0.780$

Rao et al. (2006) used the *HST*/FOS spectrum of this quasar to deduce $\log [N(\text{H I})/\text{cm}^{-2}] = 18.9^{+0.14}_{-0.11}$ for the LLS at $z = 0.78$. Higher quality reduced spectra of *HST*/FOS observations have been produced by the more recent data reduction pipelines and can be obtained from the MAST³ database (private communication, S. Rao). Hence, we downloaded the *HST*/FOS spectrum of this quasar and performed an analysis to measure the $N(\text{H I})$ associated with this LLS. The spectrum covers Lyman series absorption lines and also the Lyman limit though with a poor spectral resolution of $\sim 7 \text{ \AA}$. Our analysis resulted in a $\log [N(\text{H I})/\text{cm}^{-2}] = 19.1 \pm 0.3$. We note that our measurement remains consistent with the value reported by Rao et al. (2006) albeit with a larger uncertainty.

In Fig. 1, we present the Keck/HIRES spectrum of this quasar close to the Mg II $\lambda\lambda 2796, 2803$ and Fe II $\lambda\lambda 2344, 2374, 2586, 2600$ absorption lines at $z = 0.780$. The zero velocity is set to $z = 0.78025$ that is the systemic redshift of the host galaxy absorber (see

²<http://www.ast.cam.ac.uk/~rfc/vpfit.html>

³<https://mast.stsci.edu>

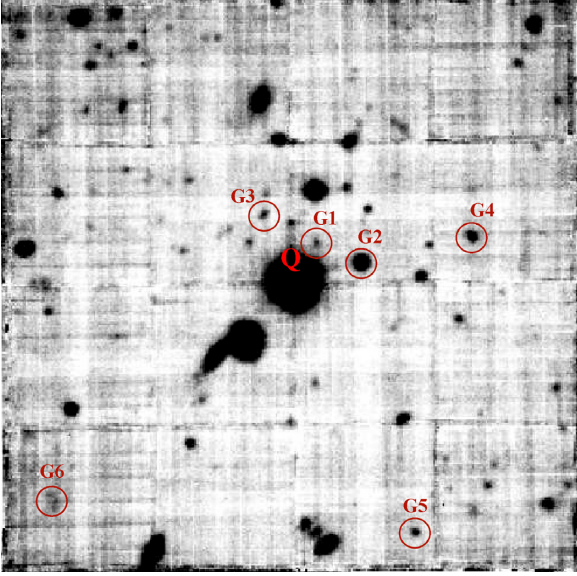


Figure 2. The $1' \times 1'$ MUSE white light image of the field of Q0152–020. The ‘G1’ to ‘G6’ letters mark the sky position of the galaxies studied in this paper, ordered by the impact parameter. ‘G2’ is associated with the absorber at $z_{\text{abs}} = 0.780$, ‘G1’, ‘G3’, and ‘G4’ are associated with the absorber at $z = 1.104$ and ‘G5’ and ‘G6’ are associated with the absorber at $z_{\text{abs}} = 1.211$. The quasar resides in the centre of the field as indicated by Q.

Section 4.1). The absorption profiles are relatively simple composed of a strong component at $v = -78 \text{ km s}^{-1}$ with a weak satellite one at $v = -103 \text{ km s}^{-1}$ that is only detected in Mg II. There are two other well-separated optically thin components at $v = -260 \text{ km s}^{-1}$ and $v = -296 \text{ km s}^{-1}$ that are detected in Mg II but not in Fe II. The best-fitting Voigt profiles to the absorption lines are shown as red continuous lines in Fig. 1. Since, the main component of the Mg II is saturated, we can only put a lower limit on its column density. The model parameters are summarized in Table 1. We further estimate the 3σ upper limits for the column density of Fe II for undetected components.

Based on the measured column density of Fe II, we obtain $[\text{Fe}/\text{H}] = -1.1 \pm 0.3$ ($[\text{X}/\text{H}] = \log(\text{X}/\text{H}) - \log(\text{X}/\text{H})_{\odot}$) where for the solar abundance we have used the value of $\log(\text{Fe}/\text{H})_{\odot} = -4.5$ (Asplund et al. 2009). The large uncertainty is due to the large error in the measured H I column density. For systems at $\log[N(\text{H I})/\text{cm}^{-2}] \sim 19$, some fraction of H and Fe are in H II and Fe III. Dessauges-Zavadsky et al. (2003) demonstrated that even in the presence of such ionized fractions the Fe II/H I ratio traces the abundance of Fe. Hence, we assume the ionization effect will not impact much our metallicity

estimate. While Fe is observed to be depleted into dust in the ISM of our Galaxy and also DLAs (Vladilo 1998; Ledoux, Bergeron & Petitjean 2002; Khare et al. 2004; Wolfe, Gawiser & Prochaska 2005; Jenkins 2009; Kulkarni et al. 2015; Jenkins & Wallerstein 2017), several studies have shown that gas associated with LLSs is dust-poor (Ménard & Fukugita 2012; Lehner et al. 2013; Fumagalli, O’Meara & Prochaska 2016). On the contrary, Meiring et al. (2009) found Fe depletion of $\gtrsim 1$ dex for two absorbers at similar $N(\text{H I})$. Therefore, while we cannot rule out the presence of the dust in this LLS, without measurements of undepleted elements like Zn we cannot quantify how dust can affect the estimated metallicity.

If dust is associated with the gas in this LLS, it can redden the spectrum of the quasar. We measure the reddening of the quasar spectrum induced by the foreground absorber by fitting a spectral template to the observed spectrum. For this purpose, we use the template by Selsing et al. (2016) and apply reddening assuming the extinction curve derived for the Small Magellanic Cloud (Gordon et al. 2003). In order to better constrain the fit, we include near-infrared photometry retrieved from archival data from 2MASS: $J = 16.74 \pm 0.06$ mag, $H = 16.64 \pm 0.08$ mag, and WISE: $W_1 = 16.71 \pm 0.03$ mag. We do not include the K band as it is contaminated by strong $\text{H}\alpha$ emission from the quasar, which we cannot constrain. Similarly, we do not include the remaining WISE photometric data as they are not covered by the spectral template. By fitting the photometry and spectrum simultaneously, we obtain a best-fitting reddening of $E(B - V) = 0.01 \pm 0.01$ mag (for a slightly redder intrinsic spectral slope of the template used in the fit: $\Delta\beta = 0.03 \pm 0.06$). For details about the fitting procedure and the definition of $\Delta\beta$, see Krogager (2015).

Since there are several absorption systems along the line of sight, the measured reddening is a strict upper limit associated with the absorption system at $z_{\text{abs}} = 0.78$. Hence, the reddening from the absorber is negligible. This can be a tentative indication of lack of dust and depletion in this LLS.

4 HOST GALAXY ABSORBERS

We searched for the [O II] nebular line emission at the redshift of each absorbing system in our MUSE datacube. Knowing the absorption redshifts, we created narrow band images at the expected observed wavelength of [O II] emission of each system and searched for the emitters. Our MUSE observation is deep enough to detect emitters with total emission line fluxes of $\gtrsim 0.5 \times 10^{-17} \text{ erg cm}^{-2} \text{ s}^{-1}$. To be complete, we also inspected the spectra of all galaxies detected only in the continuum. We note that galaxies with AB magnitudes fainter than $m_r \sim 23$ mag will not have enough SNR for redshift measurements based on their

Table 1. Metal absorption line properties of the LLS at $z = 0.78$ as extracted from the Voigt profile modelling of the Keck/HIRES spectrum of the quasar.

Component	(1)	(2)	(3)	(4)
Velocity (km s^{-1})	-78	-103	-260	-296
b (km s^{-1})	5.2 ± 0.3 $\gtrsim 14.4$	10.1 ± 2.1 12.28 ± 0.07	2.2 ± 1.1 12.17 ± 0.10	5.9 ± 1.1 12.22 ± 0.05
$\log[N(\text{Mg II})/\text{cm}^{-2}]$	13.48 ± 0.04	<12.2	<11.9	<12.0
$\log[N(\text{Fe II})/\text{cm}^{-2}]$				

Notes. Total column density of MgII: $\log[N(\text{Mg II})/\text{cm}^{-2}] \gtrsim 14.4$.
Total column density of FeII: $\log[N(\text{Fe II})/\text{cm}^{-2}] = 13.48 \pm 0.04$.
Estimated dust-uncorrected metallicity $[\text{Fe}/\text{H}] = -1.1 \pm 0.3$.

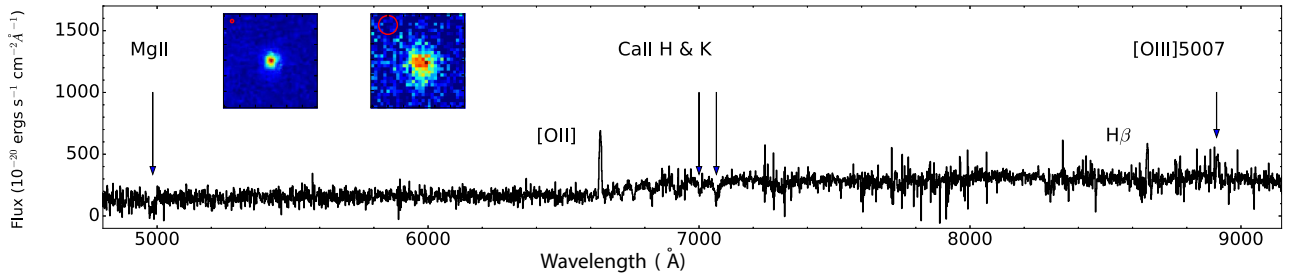


Figure 3. Extracted 1D MUSE spectrum of the LLS-galaxy at $z = 0.78025$. The $6'' \times 6''$ *HST*/WFPC2 *F702W* and [O II] MUSE narrow band postage stamp images of this galaxy are shown on the top left. A circle showing the FWHM of the seeing is included in each panel. We also detect the Mg II 2796,2803 absorption lines from the host galaxy.

Table 2. Extracted properties of G2, the host galaxy absorber at $z = 0.78$.

RA (J2000)	28.111308
Dec (J2000)	-20.017883
impact parameter (kpc)	54
z^1	0.78025 ± 0.00007
$E(B - V)$ (mag)	0.6 ± 0.1^2
dust-corrected fluxes (10^{-17} ergs s^{-1} cm^{-2})	
$f([O II])$	68 ± 19
$f(H \beta)$	19 ± 4
$f([O III]\lambda 4958)$	< 3.5
$f([O III]\lambda 5007)$	11 ± 3
Dust-corrected SFR and emission metallicity	
$SFR_{H\beta}$ ($M_{\odot} yr^{-1}$)	7 ± 2
SFR_{OII} ($M_{\odot} yr^{-1}$)	13 ± 5
Z_{em} (Z_{\odot})	0.9 ± 0.3
Metallicity gradient (dex kpc^{-1})	-0.03

Notes.

¹ Obtained by averaging the redshifts from $H\beta$ and [O III]5007 emission lines.

² See Section 4.1.3 for the details of the derivation of $E(B - V)$.

absorption features. It is worth mentioning that possible purely continuum emitting galaxies (without emission lines) below the PSF of the quasar remain undetected.

In the following, we discuss the analysis of the host galaxy absorber at $z = 0.78$. Galaxies associated with the remaining absorbing systems are presented in Appendix C. In Fig. C3, we have marked the sky position of all the galaxies studied in this work over the MUSE white light image.

4.1 Host galaxy absorber at $z_{abs} = 0.78$

We find one galaxy, G2, close to the absorption redshift at $z_{abs} = 0.78$. Fig. 3 presents the 1D spectrum of this galaxy extracted from the MUSE data cube. Strong nebular emission lines of [O II], $H\beta$, and [OIII]5007 are significantly detected. [O III]4958 is not detected but is consistent with the noise level of the flux. We use the standard deviation of the flux at the expected position of this line to find its flux upper limit. Table 2 presents the measured fluxes of different emission lines from this galaxy, including dust corrections, calculated as explained in Section 4.1.3 below. We also observe Balmer absorption at the wavelength of $H\beta$. Hence, to correctly estimate the emission line flux, we simultaneously model the profile with two Gaussian profiles to account for absorption and emission lines.

Interestingly, we also detect in absorption the Mg $\pi\lambda\lambda$ 2796,2803 doublet that can be a tracer of outflowing or inflowing gas depending

Table 3. Derived morphological parameters from the *HST*/WFPC2 *F702* image for the LLS-galaxy.

$r_{1/2}$ (kpc)	n	$\sin i$	PA (degree)
2.6 ± 0.1	1.45 ± 0.07	0.74 ± 0.01	-2 ± 2

Note. The columns of the table are: (1) half light radius; (2) Sérsic index; (3) inclination; (4) position angle

on their velocity with respect to the host galaxy (Rubin et al. 2012; Martin et al. 2012). However, the SNR in the continuum is not sufficient to study the Mg II absorption towards the host galaxy absorber.

4.1.1 Morphology from *HST*/WFPC2 broad-band imaging

We modelled the *HST*/WFPC2 *F702W* image of the host galaxy absorber at $z = 0.78$ using the surface brightness fitting tool GALFIT (Peng et al. 2010). Using a single Sérsic model, we obtained a good fit with a residual image ($\equiv [\text{model}] - [\text{data}]$) to be consistent with the background noise level with no significant feature. Hence, this galaxy does not host any bar or bulge like structure and has not experienced a recent strong interaction with possible galaxy neighbours.

The model parameters are summarized in Table 3. The Sérsic index of such a model, $n = 1.45$, indicates this galaxy has a disc-dominated morphology. We note this galaxy has a disc with a half-light radius of $0.34'' \pm 0.01''$ ($\equiv 2.6 \pm 0.1$ kpc at $z = 0.78$) and an inclination of $i = 47 \pm 1^\circ$.

4.1.2 Galaxy kinematics

To study the morphokinematics of this galaxy, we modelled the [O II] emission line using GALPAK^{3D} (Bouché et al. 2015). GALPAK^{3D} is a PYTHON-based optimization tool that simultaneously models the flux and kinematics of the emission line using a Monte Carlo Markov Chain (MCMC) algorithm. To obtain a set of robust galaxy parameters, deconvolved from seeing, GALPAK^{3D} requires the shape of the PSF which is best modelled with Moffat function as discussed in Section 2. While modelling the morphokinematics of the [OII] emission line, we assumed the wavelength ratio of the doublet to be fixed at its theoretical value of 0.9993 (Wiese, Fuhr & Deters 1996). Contini et al. (2016) demonstrated that at small inclination ($i \lesssim 50^\circ$), GALPAK^{3D} may underestimate the inclination of galaxies. Hence, to obtain a more robust parameter measurement from GALPAK^{3D}, we fixed the inclination at $i = 47^\circ$ as measured from the high spatial resolution *HST*/WFPC2 image. We allow a 10 000-long MCMC to

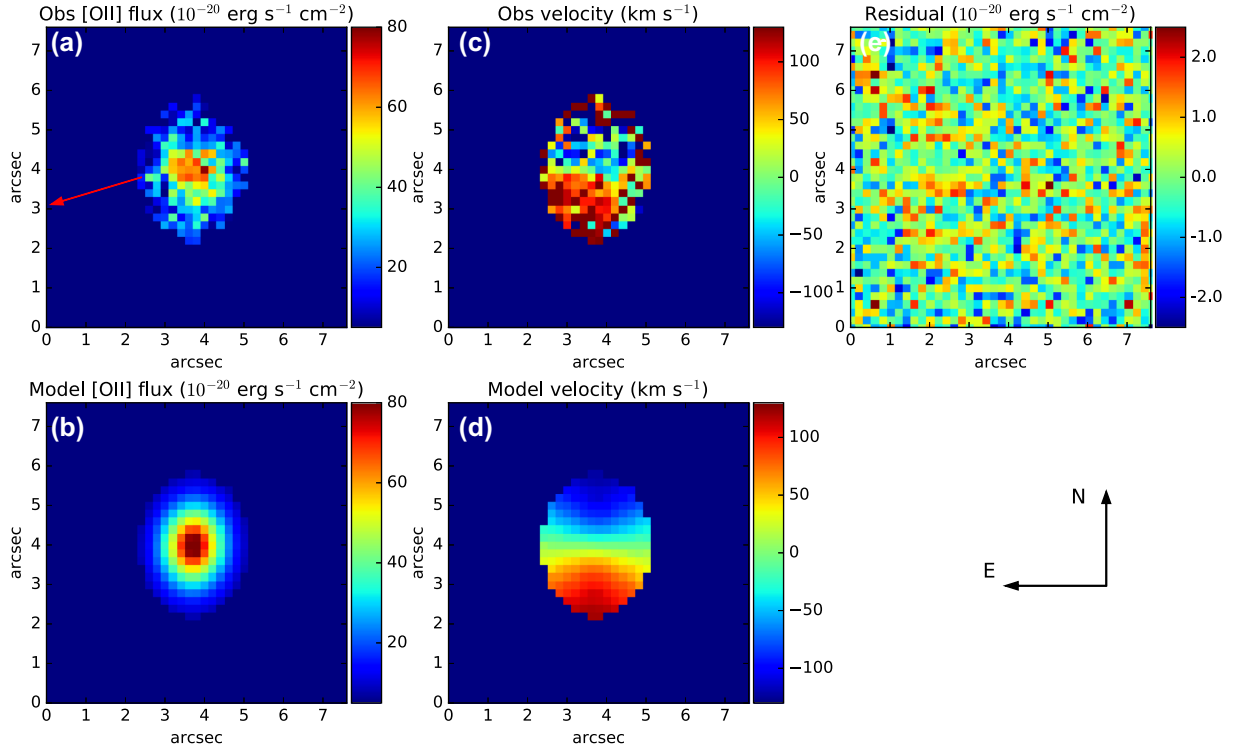


Figure 4. Observed and modeled morphokinematics of G2. (a) Observed flux map of [O II]. The red arrow indicates the direction towards the quasar. Both axes are in arcsec units, where at $z = 0.78$ the scale is 7.5 kpc/arcsec. The map presents a smooth disc-like distribution of [O II] emission without noticeable distortions. (b) The modelled flux of [O II] obtained using GALPAK^{3D}. (c,d): The observed and modelled velocity maps corresponding to the achieved model using GALPAK^{3D}. (e) The residual map (data-model) that shows the quality of the best model. The best obtained morphokinematic model has a half-light radius of $r_{1/2} = 6.7 \pm 0.2$ kpc and a rotation curve with the maximum velocity of $V_{\max} = (2.0 \pm 0.1) \times 10^2$ km s⁻¹. These translate into $M_{\text{dyn}} = (6.4 \pm 0.9) \times 10^{10} M_{\odot}$ and $M_h = (1.8 \pm 0.4) \times 10^{12} M_{\odot}$ (See Section 4.1.2 and equations (1) and (2) for the derivation of these quantities). The parameters extracted from the model are summarized in Table 4.

obtain a robust sample of the posterior probability. Also, to check the convergence of the MCMC chain, we inspect the possible correlation between each pair of parameters in their 2D distributions.

Fig. 4 shows the best morphokinematic model for G2 that is achieved using an exponential light profile along with an *arctan* rotation curve. This model corresponds to a half-light radius of $r_{1/2} = 6.7 \pm 0.2$ kpc and a maximum rotation velocity of $V_{\max} = (2.0 \pm 0.1) \times 10^2$ km s⁻¹. We estimate the enclosed mass within half-light radius using the following equation:

$$M_{\text{dyn}}(r < r_{1/2}) = r_{1/2} V_{\max}^2 / G \quad (1)$$

to be $(6.4 \pm 0.9) \times 10^{10} M_{\odot}$. Assuming a spherical virialized collapse model (Mo, Mao & White 1998):

$$M_h = 0.1 H(z)^{-1} G^{-1} V_{\max}^3, \quad (2)$$

where $H(z) = H_0 \sqrt{\Omega_{\Lambda} + \Omega_m(1+z)^3}$, we find the halo mass of this galaxy to be $M_h = (1.8 \pm 0.4) \times 10^{12} M_{\odot}$. From such a collapse model, we also obtain the $R_{\text{vir}} = 0.1 V_{\max} / H(z) = (1.9 \pm 0.1) \times 10^2$ kpc. Therefore, the sightline to the quasar, where the absorption is produced, is located at $\sim 0.3 R_{\text{vir}}$.

The measured $r_{1/2}$ of [O II] emission line obtained using GALPAK^{3D} is 2.5 ± 0.1 times larger than $r_{1/2}$ obtained for the continuum using GALFIT (see Table 3). To check if this difference is not due to the different modelling procedures or datasets, we extracted continuum narrow-band image of the galaxy from our MUSE data. Next, we used GALFIT to model this image where we found $r_{1/2} = 3.0 \pm 0.2$ kpc. This is a bit larger than the $r_{1/2}$ obtained from HST image but still consistent within 2σ . Hence, the difference between the size of the continuum emitting region and emission line region

is not due to systematic errors in our measurements. We further confirm this conclusion by modelling the [O II] narrow-band image (extracted from MUSE) using GALFIT to find $r_{1/2} = 6.2 \pm 0.4$ kpc (which is consistent with the $r_{1/2}$ from GALPAK^{3D}).

Rather, it appears that the gaseous disc of this galaxy is significantly larger than the stellar disc (e.g. see Koopmann, Haynes & Catinella 2006; Bamford, Milvang-Jensen & Arag3n-Salamanca 2007; Puech et al. 2010, for similar results but for larger samples of galaxies). While recent merger and strong SNe can be considered as two possible scenarios to provide the [O II] emitting gas surrounding galaxies, the real picture demands a study using a much larger sample of galaxies [Contini et al. (in prep.)].

There exists a tight correlation between the stellar mass and the maximum rotation velocity of galaxies, known as the stellar-mass Tully–Fisher relation (Tully & Fisher 1977). We use the reported Tully–Fisher relation for a sample of galaxies at $z \sim 0.6$ (Puech et al. 2008) and $V_{\max} = (2.0 \pm 0.1) \times 10^2$ km s⁻¹ to deduce the stellar mass of this galaxy $M_* = (3.6 \pm 1.5) \times 10^{10} M_{\odot}$ (or $\log(M_*/M_{\odot}) = 10.6 \pm 0.2$). Therefore, the stellar-mass to dark matter fraction for this halo is $2.0 \pm 0.9 \times 10^{-2}$. This is in agreement with the stellar to dark matter fraction obtained using the technique of ‘abundance matching’ which is ~ 0.02 (e.g. Behroozi, Conroy & Wechsler 2010).

4.1.3 Extinction correction

The Balmer decrement ($f(H\alpha)/f(H\beta)$) is usually used to measure the intrinsic dust extinction, $E(B - V)$, in star-forming galaxies. Since H α from this galaxy is not covered in the MUSE data cube,

Table 4. Morphokinematic parameters of G2 obtained from 3D analysis of the [O II] emission line using GALPAK^{3D}.

ID	$r_{1/2}$ (kpc)	$\sin i^1$	Position angle (degree)	Azimuthal angle (degree)	V_{\max} (km s ⁻¹)	M_{dyn} (10 ¹⁰ M _⊙)	M_{h} (10 ¹² M _⊙)	R_{vir} (kpc)	M_{\star}^2 (10 ¹⁰ M _⊙)
(1)	(2)	(3)	(4)	(5)	(6)	(7)	(8)	(9)	(10)
G2	6.7 ± 0.2	0.74	-2 ± 3	108 ± 3	(2.0 ± 0.1) × 10 ²	6.4 ± 0.9	1.8 ± 0.4	(1.9 ± 0.1) × 10 ²	3.6 ± 1.5

Note. The columns of the table are: (1) galaxy ID; (2) half-light radius; (3) sin of inclination angle; (4) position angle; (5) azimuthal angle; (6) maximum rotation velocity; (7) dynamical mass; (8) halo mass; (9) virial radius; (10) total stellar mass.

¹ The inclination was fixed at the value obtained from the *HST*/WFPC2 image of the galaxy.

² M_{\star} has been estimated using the Tully–Fisher relation (Puech et al. 2008).

we cannot directly measure the $E(B - V)$. Alternatively, Garn & Best (2010) used a large sample of galaxies in the local Universe to calibrate the total extinction for $H\alpha$, $A_{H\alpha}$, versus the stellar mass of galaxies:

$$A_{H\alpha} = \sum_{i=0}^3 B_i X^i \quad (3)$$

where $X = \log_{10}(M_{\star}/10^{10}M_{\odot})$ and B_i are the polynomial coefficients. Sobral et al. (2012) later demonstrated that the same calibration is valid at much higher redshifts, $z \sim 1.5$. Assuming that absorption-selected samples have identical dust properties to flux-limited samples, we use the same calibration and the stellar mass of this galaxy, $\log_{10}(M_{\star}/M_{\odot}) = 10.6 \pm 0.2$, to estimate the $A_{H\alpha} = 1.36 \pm 0.14$. Adopting a Small Magellanic Cloud-type (SMC-type) extinction law, we measure the $E(B - V) = 0.6 \pm 0.1$. With this value of $E(B - V)$ and the SMC extinction curve, we calculate extinction corrections to the line fluxes of [OII], $H\beta$, and [OIII]. The values listed in Table 2 include such corrections.

To obtain the dust-corrected star-formation rate (SFR), we first convert the $H\beta$ flux into $H\alpha$ flux according to the theoretical Balmer decrement (2.88) in a typical HII region. Therefore, we estimate an $H\alpha$ flux of $F(H\alpha) = (54 \pm 12) \times 10^{-17} \text{ erg s}^{-1} \text{ cm}^{-2}$. We convert the total $H\alpha$ flux of this galaxy to SFR assuming a Kennicutt (1998) conversion corrected to a Chabrier (2003) initial mass function. Using such a conversion, we find the dust-corrected SFR of this galaxy to be $7 \pm 2 M_{\odot} \text{ year}^{-1}$. We also estimate the dust-corrected SFR based on the [O II] emission using the calibration given by Kewley, Geller & Jansen (2004) to be $13 \pm 5 M_{\odot} \text{ yr}^{-1}$ which is larger than the SFR obtained based on $H\beta$ but still marginally consistent. For the remaining of the paper, we consider the SFR of these galaxies to be the average of these two estimates, $10_{-5}^{+8} M_{\odot} \text{ yr}^{-1}$. The quoted error is conservative enough to also include uncertainties via utilizing different extinction laws.

4.1.4 Emission metallicity

We deduce the oxygen abundance, O/H, of the ionized gas from the dust-corrected flux ratios of different nebular emission lines based on $R23$ index (Kobulnicky, Kennicutt & Pizagno 1999). We find the lower and upper branch values of O/H based on $R23$ as calibrated by Kobulnicky et al. (1999) to be 7.9 ± 0.2 and 8.6 ± 0.2 . Such abundances translate to $[O/H] = -0.8 \pm 0.2$ and $[O/H] = -0.1 \pm 0.2$ [$12 + \log(O/H)_{\odot} = 8.69$, Asplund et al. 2009]. However, there exists a tight correlation between the stellar mass and the metallicity of galaxies (e.g. Tremonti et al. 2004; Savaglio et al. 2005; Queyrel et al. 2009; Zahid, Kewley & Bresolin 2011; Foster et al. 2012; Yabe et al. 2015; Bian et al. 2017). Several studies have shown that galaxies with stellar masses of $\gtrsim 10^{10.5} M_{\odot}$ do not have metallicities

less than $[O/H] \sim -0.2$ (e.g. Tremonti et al. 2004; Zahid et al. 2011). Therefore, based on the stellar mass of this galaxy ($M_{\star} = 10^{10.6} M_{\odot}$) the [O/H] inferred from the upper branch, $[O/H] = -0.1 \pm 0.2$ is the preferred value for this galaxy.

Using $R23$ (and assuming we are on the upper branch), we can measure O/H at different galactocentric distances in the disc and we deduce a gradient of $\sim -0.03 \text{ dex kpc}^{-1}$. This value is consistent with the typical $\sim -0.02 \text{ dex kpc}^{-1}$ measured for the host galaxies of strong H I absorbers (e.g. Møller et al. 2013; Christensen et al. 2014; Péroux, Kulkarni & York 2014; Rahmani et al. 2016, 2018). Either value is consistent with ~ 1 dex difference between emission-based O/H and absorption-based Fe/H at an impact parameter 54 kpc, if the gradient continues at this rate all the way to 54 kpc. While this agreement is suggestive, we do note that later (Section 5.1) we discount an extended disc origin for the absorber on kinematic grounds.

In comparing the absorption and emission abundances, we have assumed that O/Fe is solar. This may be an invalid assumption in this star-forming galaxy, since the generation of core-collapse SN from massive stars can lead to O/Fe values that are two to three times larger than that of solar. We note however, this is still not enough to explain the observed difference between the abundances of the two gas phases. However, it is worth noting that the effect of dust depletion can be large to explain the observed metallicity difference. However, as noted earlier, we cannot quantify it in this absorber.

5 NATURE OF THE ABSORBING GAS AT z

ABS = 0.78

We have detected the host galaxy absorber of an LLS at $z = 0.78$ at an impact parameter of $b = 54 \text{ kpc}$. In the following, we study the possible nature of this LLS.

5.1 Galaxy disc

This LLS may originate from the gas associated with the extended disc of the galaxy. This scenario is supported by the disc-like morphology of the galaxy and the fact that the extrapolated metallicity of the galaxy is consistent with the absorption metallicity. In such a scenario, one expects the LLS line of sight velocity to match the one predicted from the rotation curve of the galaxy (Chen, Kennicutt & Rauch 2005; but see Neeleman et al. 2016 for a counter-example). As indicated in panel **c** of Fig. 4, the rotation of the disc towards the quasar sightline would produce a redshifted velocity with respect to the systemic velocity of the galaxy. To be more precise, we use the best morphokinematic model of the galaxy obtained from GALPAK^{3D} and extrapolate it to the position of the quasar. The projected velocity at the apparent position of the quasar is $v_Q = 50 \pm 10 \text{ km s}^{-1}$.

Given the large velocity differences ($\delta v > 130 \text{ km s}^{-1}$) between the disc and absorption components (located at $v \sim -80 \text{ km s}^{-1}$ and $v \sim -300 \text{ km s}^{-1}$ —see Section 3.1), we conclude that this LLS is not associated with the disc of the galaxy.

Azimuthal angle, ϕ , in quasar–galaxy pairs is defined to be the angle between the galaxy major axis and the quasar line of sight. At $\phi \approx 90^\circ$, the sightline towards the quasar probes the galaxy poles while at $\phi \approx 0^\circ$ it passes close to the galactic disc. We have measured $\phi = 70^\circ$ for this quasar–galaxy pair that shows the sightlines probe the regions far from the galaxy disc. This consideration further argues against the disc scenario as the possible origin of the absorbing gas.

5.2 Warped disc

Warped extended discs, that can be inclined up to $\sim 20^\circ$ with respect to the stellar disc, are commonly observed to be associated with disc galaxies in the local Universe (e.g. Briggs 1990; García-Ruiz, Sancisi & Kuijken 2002; Heald et al. 2011). Galactic warps are usually detected at a few effective radii but in extreme cases have also been seen to extend up to $\sim 60 \text{ kpc}$. There also exists observational evidence of warped discs at higher redshifts (Bouché et al. 2013; Burchett et al. 2013; Diamond-Stanic et al. 2016; Rahmani et al. 2018). Gas accretion is considered as one of the most plausible explanation for the presence of such structures (Stewart et al. 2011; Shen et al. 2013; Stewart et al. 2017). Due to the large velocity difference of the LLS with respect to the disc and the azimuthal angle of $\phi = 70^\circ$, we reject such a scenario for the nature of the LLS as galactic warps are expected to corotate with the galaxy discs, though with only a small lag.

5.3 High-velocity clouds

High-velocity clouds (HVCs) associated with the CGM of our Galaxy are defined as gaseous structures with $|v_{\text{LSR}}| \gtrsim 90 \text{ km s}^{-1}$ (Wakker & van Woerden 1997). HVCs are also observed in the CGM of other galaxies in the Local group with similar $N(\text{H I})$ and metallicities as this LLS (e.g. Lehner & Howk 2010; Lehner et al. 2012; Richter et al. 2016). The majority of the HVCs in the Milky Way reside within $b = 15 \text{ kpc}$ (Wakker et al. 2007, 2008) which is $\simeq 4$ times smaller than the impact parameter of this LLS ($b = 54 \text{ kpc}$). HVCs associated with tidal streams of the LMC have been found at larger distances of up to $\sim 50 \text{ kpc}$ and with velocities as large as 300 km s^{-1} . In the case of M31, HVCs are observed up to distances of 150 kpc that may not be related to any tidal interaction (Westmeier, Braun & Thilker 2005; Westmeier et al. 2007; Wolfe, Lockman & Pisano 2016). Therefore, both the strong component at $v \sim -80 \text{ km s}^{-1}$ and the two weaker ones at $v \sim -300 \text{ km s}^{-1}$ may originate from HVC-like structures in the CGM of this galaxy.

5.4 Galactic wind

The azimuthal angle of $\phi = 70^\circ$ between Q0152–020 and G2 indicates that the quasar sightline probes closer to the galactic pole where galactic winds are expected to reside (e.g. Bouché et al. 2012; Kacprzak, Churchill & Nielsen 2012). By dividing the dust-corrected SFR of $10^{+8}_{-5} M_\odot \text{ yr}^{-1}$ by the surface of $\pi r_{1/2}^2$, where $r_{1/2} = 6.7 \pm 0.2 \text{ kpc}$, we measure the average SFR surface density of $\Sigma_{\text{SFR}} = 0.07^{+0.06}_{-0.04} M_\odot \text{ yr}^{-1} \text{ kpc}^{-2}$. This Σ_{SFR} is consistent with the threshold of $\Sigma_{\text{SFR}} \gtrsim 0.1 M_\odot \text{ yr}^{-1} \text{ kpc}^{-2}$ required for driving large-

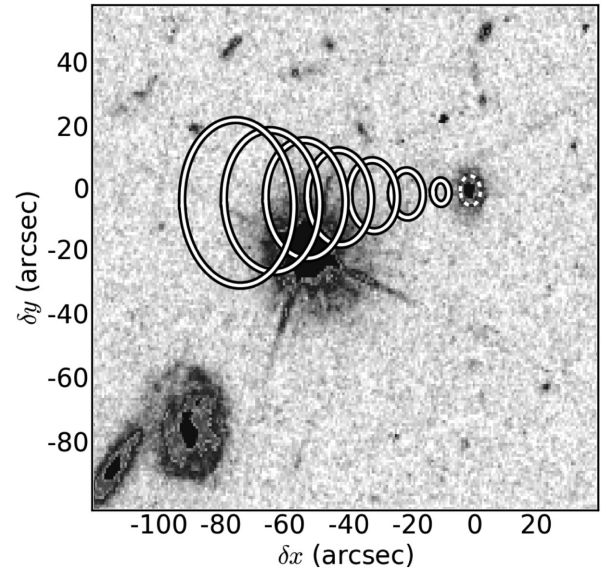


Figure 5. Representation of the cone model utilized to reproduce the quasar absorption line spectrum. *top*: Zoomed *HST*/WFPC2 image over which the cone model is illustrated in the sky plane (xy). The dashed and inclined circles, respectively, indicate the galaxy disc and the wind cone. *bottom* (B1): Normalized Keck/HIRES quasar spectrum close to the Fe II 2344 absorption line. *bottom* (B2): The reconstructed profile based on the galactic wind cone model. The best match to the observed spectrum is obtained with a wind velocity of $V_w = 110 \text{ km s}^{-1}$ and a cone opening angle of $\theta_{\text{max}} = 15^\circ$.

scale galactic winds (Heckman 2002; Newman et al. 2012; Bordoloi et al. 2014a).

In order to see if this LLS can be associated with a galactic wind, we try to reproduce the absorption lines by utilizing a wind cone model as described in Bouché et al. (2012) (and also in Schroetter et al. 2015, 2016). In such a wind model one assumes a cone, with an opening angle θ_{max} ,⁴ filled with randomly distributed gas clouds decreasing in number as $1/r^2$, r being the distance from the centre of the galaxy. The clouds in this model are quickly accelerated to their terminal velocity V_w in a few kpc ($< 10 \text{ kpc}$). The projection of the velocity of particles in the cone, onto the quasar sightline, provides us with an optical depth τ_v which is then turned into a simulated absorption profile. The comparison with the observed absorption line is finally carried out after convolving the simulated profile with the instrumental line spread function and adding to it Poisson noise in order to reproduce the instrumental noise.

We achieved the best match between the simulated and observed absorption profiles with a wind velocity of $V_w = 110 \pm 4 \text{ km s}^{-1}$ and a cone opening angle of $\theta_{\text{max}} = 15 \pm 2^\circ$. We show a schematic representation of such a model in the *top* panel of Fig. 5 where the cone is oriented to be perpendicular to the disc of the galaxy. In the *bottom* panels of Fig. 5 we present the observed (panel B1) and simulated (panel B2) spectra of Fe II 2344 which verifies that such a wind model can reproduce the main absorption component of the LLS.

Using the wind velocity and the cone opening angle, we can now derive the ejected mass rate of the wind, \dot{M}_{out} , by using equation (1)

⁴ θ_{max} is defined from the central axis, and the cone subtends an area Σ of $\pi \cdot \theta_{\text{max}}^2$.

of Schroetter et al. (2015):

$$\dot{M}_{\text{out}} = \mu \cdot N_{\text{H}}(b) \cdot b \cdot V_w \cdot \frac{\pi}{2} \cdot \theta_{\text{max}}, \quad (4)$$

where μ is the mean atomic weight, b the impact parameter, θ_{max} the cone opening angle, V_w the wind velocity, and $N_{\text{H}}(b)$ the hydrogen column density at the distance b . Using equation (4) and assuming $\mu = 1.5$, we find an $\dot{M}_{\text{out}} = 0.38_{-0.10}^{+0.15} M_{\odot} \text{ yr}^{-1}$. Since some fraction of hydrogen in LLSs is ionized (e.g. Dessauges-Zavadsky et al. 2003; Lehner et al. 2013; Fumagalli et al. 2016; Prochaska et al. 2017), this mass ejection rate should be considered as a lower limit. Assuming a symmetry for the wind geometry (i.e. two cones of ejecting gas from both sides of the galaxy), the mass ejection rate would be twice that. From the value of the ejected mass rate of both cones, we can derive the loading factor η , defined as $\dot{M}_{\text{out}}/\text{SFR}$. With the \dot{M}_{out} of $\gtrsim 0.8 M_{\odot} \text{ yr}^{-1}$ we find a loading factor $\eta \gtrsim 0.1$.

We further derive the escape velocity $V_{\text{esc}}(b)$ of the halo at a distance b from the host galaxy assuming an isothermal sphere profile given by Veilleux, Cecil & Bland-Hawthorn (2005):

$$V_{\text{esc}} = V_{\text{max}} \times \sqrt{2 \left[1 + \ln \left(\frac{R_{\text{vir}}}{r} \right) \right]}, \quad (5)$$

where V_{max} is the maximum rotation velocity of the galaxy and R_{vir} is the virial radius. With a $V_{\text{max}} = (2.0 \pm 0.1) \times 10^2 \text{ km s}^{-1}$ and $R_{\text{vir}} = (1.9 \pm 0.1) \times 10^2 \text{ kpc}$, we find an escape velocity of $V_{\text{esc}} \simeq 430 \text{ km s}^{-1}$. This value is approximately four times larger than the wind velocity. Therefore, such a wind cannot escape the gravitational potential of the halo. The estimated escape velocity assuming a Navarro–Frenk–White (so called NFW) profile (Navarro, Frenk & White 1996) for the halo is 250 km s^{-1} which is ~ 1.7 times smaller than the value deduced above for an isothermal sphere. However, the main conclusion remains unchanged since such an escape velocity is still ~ 2.3 times larger than the wind speed.

We further explored if the wind cone model can explain the origin of the other, weaker, absorption components (see Fig. 1). However, within a reasonable range of parameters for V_w and θ_{max} we were not able to reproduce such absorption profiles. Hence, the remaining components may not originate in a wind associated with this galaxy.

It is worth noting that the measured metallicity from the emission lines is ~ 1 dex larger than that obtained from the gas seen in absorption. This appears to be inconsistent with the wind picture in which one expects to observe higher or equal metallicity gas in absorption compared to that of the host galaxy. However, the overproduction of O compared to Fe due to core-collapse SN and the dust depletion of Fe can reduce the metallicity difference significantly. Moreover, cosmological hydrodynamical simulations predict a significant mixing of the wind materials at large radii ($\gtrsim 0.25 R_{\text{vir}}$) with the pristine accreted gas from IGM that significantly dilutes the wind metallicity (e.g. Mitchell et al. 2017; Muratov et al. 2017).

6 SUMMARY AND CONCLUSION

In this work, we have studied an LLS with $\log [N(\text{H})/\text{cm}^{-2}] = 19.1 \pm 0.3$ at $z = 0.78$ towards Q0152–020. The metal absorption profiles associated with this LLS consist of a strong main component (seen in Mg II and Fe II) but also another two well-separated weaker components at velocity differences of $\sim 200 \text{ km s}^{-1}$ (that are only detected in Mg II). We have measured a dust-uncorrected absorption metallicity of $[\text{Fe}/\text{H}] = -1.1 \pm 0.3$ dex.

At the absorption redshift of $z_{\text{abs}} = 0.78$, our VLT/MUSE data is sensitive to a dust-uncorrected SFR = $0.5 M_{\odot} \text{ yr}^{-1}$. Inspecting our

VLT/MUSE data, we find one galaxy at a velocity separation of $v = 78 \text{ km s}^{-1}$ with respect to the main absorption component. This galaxy is located at an impact parameter of $b = 54 \text{ kpc}$. We confirm the redshift of this galaxy by detecting [O II], [O III]5007, and H β emission lines.

By modelling the *HST*/WFPC2 F702 broad-band image of this galaxy using a Sérsic profile, we obtained a fit with $n = 1.45 \pm 0.07$. The morphokinematic modelling, using the MUSE data cube, shows this galaxy has a rotation curve with a $V_{\text{max}} = (2.0 \pm 0.1) \times 10^2 \text{ km s}^{-1}$. Such analyses further lead us to conclude that this discy galaxy has not suffered from recent strong interactions with other galaxies.

We infer the stellar mass using the Tully–Fisher relation to be $M_{\star} = (3.6 \pm 1.5) \times 10^{10} M_{\odot}$. We further measure a dust-corrected SFR for this galaxy to be $10_{-5}^{+8} M_{\odot} \text{ yr}^{-1}$ and oxygen abundance of $[\text{O}/\text{H}] = -0.1 \pm 0.2$. We also estimate a metallicity gradient of $\sim 0.03 \text{ dex kpc}^{-1}$.

At the position of the quasar, the predicted velocity of gas corotating with the disc of the galaxy is $+50 \text{ km s}^{-1}$. Since the velocities of different absorbing components are $v \sim -80 \text{ km s}^{-1}$ and $v \sim -300 \text{ km s}^{-1}$ we reject a scenario in which the LLS originates from the stellar disc or a warped disc associated with this galaxy.

HVCs, associated with the galaxies in the Local group, have similar metallicities and velocities to this LLS and can be found at comparable impact parameters to their host galaxies. Hence, we cannot refute the possibility that one or more absorption components can be associated with HVC-like clouds in the CGM of the host galaxy.

We also explore the possibility that the LLS arises from a galactic wind phenomenon. This model is supported by the azimuthal angle of $\phi = 70^\circ$ which shows the quasar sightline passes close to the galactic pole. We try to reproduce the absorption profile using a wind model where gas clouds are confined within a cone and have reached their terminal velocity. A good match to the absorption profile of one of the absorption components is achieved with a wind velocity of $V_w = 110 \pm 4 \text{ km s}^{-1}$ and cone opening angle of $\theta_{\text{max}} = 15 \pm 2^\circ$. We estimate a total mass ejection rate of $\dot{M} \gtrsim 0.8 M_{\odot} \text{ yr}^{-1}$ and a loading factor of $\eta \gtrsim 0.1$. This parameter plays a crucial role in reproducing the observed population of galaxies in simulations (e.g. Dutton 2012; Davé et al. 2013; Muratov et al. 2015; Hayward & Hopkins 2017). However, our estimated value of $\eta \gtrsim 0.1$ is in agreement with those from FIRE simulations (Muratov et al. 2015). We further find the escape velocity from the halo of this galaxy is almost four times larger than the wind speed. Therefore, this outflowing material will not be able to leave the halo of this galaxy.

Guillemin & Bergeron (1997) had also searched for the host galaxy of this absorbing system where they associated it with a galaxy at $z = 0.603$ ($\Delta v \gtrsim 3 \times 10^5 \text{ km s}^{-1}$). Thanks to the large field of view and the high-sensitivity of MUSE, we can now reliably identify and study the host galaxy absorber. Further combining MUSE data with the high spectral resolution quasar absorption line data and *HST* image of the field, we further studied the nature of the absorbing gas. Altogether, our results show the power of IFU observations of quasar–galaxy pairs in CGM studies.

ACKNOWLEDGEMENTS

HR thanks Francois Hammer, Mathieu Puech, and Hector Flores for useful suggestions. CP was supported by an ESO science visitor programme and the DFG cluster of excellence ‘Origin and Structure of the Universe’. This work has been carried out thanks to the support of the OCEVU Labex (ANR-11-LABX-0060) and the A*MIDEX

project (ANR-11-IDEX-0001-02) funded by the ‘Investissements d’Avenir’ French government program managed by the ANR. This research was supported by the DFG cluster of excellence ‘Origin and Structure of the Universe’ (www.universe-cluster.de). RA thanks ESO and CNES for the support of her PhD. VPK gratefully acknowledges partial support from a NASA/STScI grant for program GO 13801, and additional support from NASA grants NNX14AG74G and NNX17AJ26G. The research leading to these results has received funding from the French Agence Nationale de la Recherche under grant no ANR-17-CE31-0011-01.

REFERENCES

- Asplund M., Grevesse N., Sauval A. J., Scott P., 2009, *ARA&A*, 47, 481
- Bacon R. et al., 2015, *A&A*, 575, A75
- Bamford S. P., Milvang-Jensen B., Aragón-Salamanca A., 2007, *MNRAS*, 378, L6
- Behroozi P. S., Conroy C., Wechsler R. H., 2010, *ApJ*, 717, 379
- Bian F., Kewley L. J., Dopita M. A., Blanc G. A., 2017, *ApJ*, 834, 51
- Bordoloi R. et al., 2014a, *ApJ*, 794, 130
- Bordoloi R. et al., 2014b, *ApJ*, 796, 136
- Bordoloi R., Rigby J. R., Tumlinson J., Bayliss M. B., Sharon K., Gladders M. G., Wuyts E., 2016, *MNRAS*, 458, 1891
- Borthakur S., Heckman T., Strickland D., Wild V., Schiminovich D., 2013, *ApJ*, 768, 18
- Bouché N., Murphy M. T., Péroux C., Davies R., Eisenhauer F., Förster Schreiber N. M., Tacconi L., 2007, *ApJ*, 669, L5
- Bouché N., Hohensee W., Vargas R., Kacprzak G. G., Martin C. L., Cooke J., Churchill C. W., 2012, *MNRAS*, 426, 801
- Bouché N., Murphy M. T., Kacprzak G. G., Péroux C., Contini T., Martin C. L., Dessauges-Zavadsky M., 2013, *Science*, 341, 50
- Bouché N., Carfantan H., Schroetter I., Michel-Dansac L., Contini T., 2015, *AJ*, 150, 92
- Briggs F. H., 1990, *ApJ*, 352, 15
- Burchett J. N., Tripp T. M., Werk J. K., Howk J. C., Prochaska J. X., Ford A. B., Davé R., 2013, *ApJ*, 779, L17
- Chabrier G., 2003, *PASP*, 115, 763
- Chen H.-W., Kennicutt R. C., Jr, Rauch M., 2005, *ApJ*, 620, 703
- Christensen L., Møller P., Fynbo J. P. U., Zafar T., 2014, *MNRAS*, 445, 225
- Contini T. et al., 2016, *A&A*, 591, A49
- Davé R., Katz N., Oppenheimer B. D., Kollmeier J. A., Weinberg D. H., 2013, *MNRAS*, 434, 2645
- Dessauges-Zavadsky M., Péroux C., Kim T.-S., D’Odorico S., McMahon R. G., 2003, *MNRAS*, 345, 447
- Diamond-Stanic A. M., Coil A. L., Moustakas J., Tremonti C. A., Sell P. H., Mendez A. J., Hickox R. C., Rudnick G. H., 2016, *ApJ*, 824, 24
- Dutton A. A., 2012, *MNRAS*, 424, 3123
- Ellison S. L., Kewley L. J., Mallén-Ornelas G., 2005, *MNRAS*, 357, 354
- Erb D. K., 2015, *Nature*, 523, 169
- Finley H. et al., 2017, *A&A*, 605, A118
- Foster C. et al., 2012, *A&A*, 547, A79
- Frank S. et al., 2012, *MNRAS*, 420, 1731
- Fumagalli M., O’Meara J. M., Prochaska J. X., 2016, *MNRAS*, 455, 4100
- García-Ruiz I., Sancisi R., Kuijken K., 2002, *A&A*, 394, 769
- Garn T., Best P. N., 2010, *MNRAS*, 409, 421
- Goldoni P., 2011, *Astron. Nachrichten*, 332, 227
- Gordon K. D., Clayton G. C., Misselt K. A., Landolt A. U., Wolff M. J., 2003, *ApJ*, 594, 279
- Guillemin P., Bergeron J., 1997, *A&A*, 328, 499
- Hafen Z. et al., 2017, *MNRAS*, 469, 2292
- Hayward C. C., Hopkins P. F., 2017, *MNRAS*, 465, 1682
- Heald G. et al., 2011, *A&A*, 526, A118
- Heckman T. M., 2002, in Mulchaey J. S., Stocke J. T., eds, *Astronomical Society of the Pacific Conference Series Vol. 254, Extragalactic Gas at Low Redshift*, p. 292
- Hinshaw G. et al., 2013, *ApJS*, 208, 19
- Jenkins E. B., 2009, *ApJ*, 700, 1299
- Jenkins E. B., Wallerstein G., 2017, *ApJ*, 838, 85
- Kacprzak G. G., Churchill C. W., Steidel C. C., Murphy M. T., Evans J. L., 2007, *ApJ*, 662, 909
- Kacprzak G. G., Churchill C. W., Nielsen N. M., 2012, *ApJ*, 760, L7
- Kacprzak G. G. et al., 2014, *ApJ*, 792, L12
- Kennicutt R. C., Jr, 1998, *ARA&A*, 36, 189
- Kewley L. J., Geller M. J., Jansen R. A., 2004, *AJ*, 127, 2002
- Khare P., Kulkarni V. P., Lauroesch J. T., York D. G., Crotts A. P. S., Nakamura O., 2004, *ApJ*, 616, 86
- Kobulnicky H. A., Kennicutt R. C., Jr, Pizagno J. L., 1999, *ApJ*, 514, 544
- Koopmann R. A., Haynes M. P., Catinella B., 2006, *AJ*, 131, 716
- Krogager J.-K., 2015, PhD thesis, University of Copenhagen, Denmark ([arXiv:1604.06230](https://arxiv.org/abs/1604.06230))
- Krogager J.-K., Fynbo J. P. U., Møller P., Ledoux C., Noterdaeme P., Christensen L., Milvang-Jensen B., Sparre M., 2012, *MNRAS*, 424, L1
- Kulkarni V. P., Meiring J., Som D., Péroux C., York D. G., Khare P., Lauroesch J. T., 2012, *ApJ*, 749, 176
- Kulkarni V. P., Som D., Morrison S., Peroux C., Quiret S., York D. G., 2015, *ApJ*, 815, 24
- Ledoux C., Bergeron J., Petitjean P., 2002, *A&A*, 385, 802
- Lehner N., Howk J. C., 2010, *ApJ*, 709, L138
- Lehner N., Howk J. C., Thom C., Fox A. J., Tumlinson J., Tripp T. M., Meiring J. D., 2012, *MNRAS*, 424, 2896
- Lehner N. et al., 2013, *ApJ*, 770, 138
- Martin C. L., Shapley A. E., Coil A. L., Kornei K. A., Bundy K., Weiner B. J., Noeske K. G., Schiminovich D., 2012, *ApJ*, 760, 127
- Meiring J. D., Lauroesch J. T., Kulkarni V. P., Péroux C., Khare P., York D. G., 2009, *MNRAS*, 397, 2037
- Ménard B., Fukugita M., 2012, *ApJ*, 754, 116
- Mitchell P., Blaizot J., Devriendt J., Kimm T., Michel-Dansac L., Rosdahl J., Slyz A., 2018, *MNRAS*, 474, 492
- Mo H. J., Mao S., White S. D. M., 1998, *MNRAS*, 295, 319
- Monier E. M., Turnshek D. A., Rao S., 2009, *MNRAS*, 397, 943
- Muratov A. L., Kereš D., Faucher-Giguère C.-A., Hopkins P. F., Quataert E., Murray N., 2015, *MNRAS*, 454, 2691
- Muratov A. L. et al., 2017, *MNRAS*, 468, 4170
- Møller P., Warren S. J., 1998, *MNRAS*, 299, 661
- Møller P., Fynbo J. P. U., Ledoux C., Nilsson K. K., 2013, *MNRAS*, 430, 2680
- Møller P. et al., 2018, *MNRAS*, 474, 4039
- Navarro J. F., Frenk C. S., White S. D. M., 1996, *ApJ*, 462, 563
- Neeleman M. et al., 2016, *ApJ*, 820, L39
- Newman S. F. et al., 2012, *ApJ*, 761, 43
- Noterdaeme P., Petitjean P., Ledoux C., Srianand R., 2009, *A&A*, 505, 1087
- Noterdaeme P. et al., 2012a, *A&A*, 540, A63
- Noterdaeme P. et al., 2012b, *A&A*, 547, L1
- O’Meara J. M. et al., 2015, *AJ*, 150, 111
- Peng C. Y., Ho L. C., Impey C. D., Rix H.-W., 2010, *AJ*, 139, 2097
- Péroux C., McMahon R. G., Storrle-Lombardi L. J., Irwin M. J., 2003, *MNRAS*, 346, 1103
- Péroux C., Bouché N., Kulkarni V. P., York D. G., Vladilo G., 2011a, *MNRAS*, 410, 2237
- Péroux C., Bouché N., Kulkarni V. P., York D. G., Vladilo G., 2011b, *MNRAS*, 410, 2251
- Péroux C., Kulkarni V. P., York D. G., 2014, *MNRAS*, 437, 3144
- Péroux C. et al., 2017, *MNRAS*, 464, 2053
- Pettini M., Rix S. A., Steidel C. C., Adelberger K. L., Hunt M. P., Shapley A. E., 2002, *ApJ*, 569, 742
- Piqueras L., Conseil S., Shepherd M., Bacon R., Leclercq F., Richard J., 2017, preprint ([arXiv:1710.03554](https://arxiv.org/abs/1710.03554))
- Prochaska J. X., Herbert-Fort S., Wolfe A. M., 2005, *ApJ*, 635, 123
- Prochaska J. X. et al., 2017, *ApJ*, 837, 169
- Puech M. et al., 2008, *A&A*, 484, 173
- Puech M., Hammer F., Flores H., Delgado-Serrano R., Rodrigues M., Yang Y., 2010, *A&A*, 510, A68
- Queyrel J. et al., 2009, *A&A*, 506, 681

- , Quiret S. et al., 2016, *MNRAS*, 458, 4074
 Rahmani H., Srianand R., Noterdaeme P., Petitjean P., 2010, *MNRAS*, 409, L59
 Rahmani H. et al., 2016, *MNRAS*, 463, 980
 Rahmani H. et al., 2018, *MNRAS*, 474, 254
 Rao S. M., Turnshek D. A., Nestor D. B., 2006, *ApJ*, 636, 610
 Rao S. M., Belfort-Mihalji M., Turnshek D. A., Monier E. M., Nestor D. B., Quider A., 2011, *MNRAS*, 416, 1215
 Richter P. et al., 2017, *ApJ*, 607, 48
 Rubin K. H. R., Prochaska J. X., Koo D. C., Phillips A. C., 2012, *ApJ*, 747, L26
 Sargent W. L. W., Boksenberg A., Steidel C. C., 1988a, *ApJS*, 68, 539
 Sargent W. L. W., Steidel C. C., Boksenberg A., 1988b, *ApJ*, 334, 22
 Savaglio S. et al., 2005, *ApJ*, 635, 260
 Schroetter I., Bouché N., Péroux C., Murphy M. T., Contini T., Finley H., 2015, *ApJ*, 804, 83
 Schroetter I. et al., 2016, *ApJ*, 833, 39
 Selsing J., Fynbo J. P. U., Christensen L., Krogager J.-K., 2016, *A&A*, 585, A87
 Shen S., Madau P., Guedes J., Mayer L., Prochaska J. X., Wadsley J., 2013, *ApJ*, 765, 89
 Shull J. M., 2014, *ApJ*, 784, 142
 Sobral D., Best P. N., Matsuda Y., Smail I., Geach J. E., Cirasuolo M., 2012, *MNRAS*, 420, 1926
 Steidel C. C., Erb D. K., Shapley A. E., Pettini M., Reddy N., Bogosavljević M., Rudie G. C., Rakic O., 2010, *ApJ*, 717, 289
 Stewart K. R., Kaufmann T., Bullock J. S., Barton E. J., Maller A. H., Diemand J., Wadsley J., 2011, *ApJ*, 738, 39
 Stewart K. R. et al., 2017, *ApJ*, 843, 47
 Tremonti C. A. et al., 2004, *ApJ*, 613, 898
 Tully R. B., Fisher J. R., 1977, *A&A*, 54, 661
 Veilleux S., Cecil G., Bland-Hawthorn J., 2005, *ARA&A*, 43, 769
 Vernet J. et al., 2011, *A&A*, 536, A105
 Vladilo G., 1998, *ApJ*, 493, 583
 Wakker B. P., van Woerden H., 1997, *ARA&A*, 35, 217
 Wakker B. P. et al., 2007, *ApJ*, 670, L113
 Wakker B. P., York D. G., Wilhelm R., Barentine J. C., Richter P., Beers T. C., Ivezić Ž., Howk J. C., 2008, *ApJ*, 672, 298
 Westmeier T., Braun R., Thilker D., 2005, *A&A*, 436, 101
 Westmeier T., Braun R., Brüns C., Kerp J., Thilker D. A., 2007, *New A Rev.*, 51, 108
 Wiese W. L., Fuhr J. R., Deters T. M., 1996, Atomic transition probabilities of carbon, nitrogen, and oxygen : a critical data compilation
 Wolfe A. M., Gawiser E., Prochaska J. X., 2005, *ARA&A*, 43, 861
 Wolfe S. A., Lockman F. J., Pisano D. J., 2016, *ApJ*, 816, 81
 Wotta C. B., Lehner N., Howk J. C., O'Meara J. M., Prochaska J. X., 2016, *ApJ*, 831, 95
 Yabe K. et al., 2015, *PASJ*, 67, 102
 Zafar T., Péroux C., Popping A., Milliard B., Deharveng J.-M., Frank S., 2013, *A&A*, 556, A141
 Zahid H. J., Kewley L. J., Bresolin F., 2011, *ApJ*, 730, 137

APPENDIX A: NEW X-SHOOTER OBSERVATIONS

Q0152–020 has been observed with VLT/X-Shooter (Vernet et al. 2011) under the ESO program 095.A-0338 (PI: Péroux). The X-Shooter spectrograph covers a wavelength range of 0.3 μm to 2.3 μm at medium resolution in a simultaneous use of three arms in UVB, VIS, and NIR. For a robust sky subtraction, the nodding mode was used following the ABBA scheme with the default nod length (2.5"). Slit widths of 1.0", 0.9", and 0.9" were used for, respectively, UVB, VIS, and NIR arms. These choices of slit widths result in formal spectral resolving powers of 5100, 8800, and 5600 for the UVB, VIS, and NIR respectively.

To reduce the raw data, we used the X-Shooter pipeline version 2.2.0⁵ (Goldoni 2011). We followed a standard procedure of X-Shooter data reduction to obtain the 1D spectrum of the quasar (Rahmani et al. 2016). We first made an initial estimate for the wavelength solution and position of the centre and edges of each order. Then, we obtained the accurate position of the centre of echelle orders and followed this step by generating the master flat frame out of five individual lamp exposures. Next, the 2D wavelength solution was found and modified by applying a flexure correction. Finally, we subtracted each pair of nods to obtain the flat-fielded, wavelength-calibrated, and sky-subtracted 2D spectrum. As we are primarily interested in studying the (narrow) absorption lines, we did not attempt to flux-calibrate the spectrum.

APPENDIX B: PROPERTIES OF OTHER ABSORBING SYSTEMS TOWARDS Q0152–020

In this section, we present the absorption line properties of absorbing systems towards Q0152–020 at $1 < z < 1.5$. In Table C1, we summarize the column density measurements for different ions. We do not detect the Ly α absorption line to be associated with any of these absorbers. Hence, we estimated upper limits on $N(H\text{I})$ from the *HST*/FOS data.

B1 Absorbing system at $z_{\text{abs}} = 1.104$

The Keck/HIRES spectrum of Q0152–020 presents a single-component Mg II absorbing system at $z_{\text{abs}} = 1.104$ with no detectable associated Fe II absorption line. Also, at the same redshift, we find a C IV absorbing system. The C IV absorption lines consist of two components where one is located at the velocity of the Mg II but the second at a $\Delta v = 216 \text{ km s}^{-1}$. These metal absorption lines are shown in Fig. B1. The histogram and the red continuous lines indicate the observed spectrum and the Voigt profile fits, respectively.

B2 Absorbing system at $z_{\text{abs}} = 1.211$

Neither from the Keck/HIRES spectrum nor from the VLT/X-Shooter do we detect Fe II absorption lines associated with this Mg II system. However, there exists a strong C IV absorption at the same redshift. Fig. B2 shows the VLT/X-Shooter spectrum of this absorbing system. The best-fitting Voigt profile consists of two components for MgII and a single one for C IV. In passing, we note that the higher resolution C IV profile from Keck/HIRES spectrum also does not present any velocity structure as it is fully saturated.

B3 Absorbing system at $z_{\text{abs}} = 1.224$

Keck/HIRES spectrum of Q0152–020 presents a strong C IV absorber at $z_{\text{abs}} = 1.224$. Neither in the X-Shooter spectrum nor in the Keck/HIRES spectrum do we detect any of the singly ionized species to be associated with this system. Fig. B3 shows the Keck/HIRES spectrum close to the C IV absorption lines. We modelled the absorption profile using three Voigt profile components spread over 220 km s^{-1} .

B4 absorbing system at $z_{\text{abs}} = 1.480$

We do not find any of the singly ionized species to be associated with this relatively weak C IV absorber at $z_{\text{abs}} = 1.480$. The best-fitting

⁵<http://www.eso.org/sci/software/pipelines/>

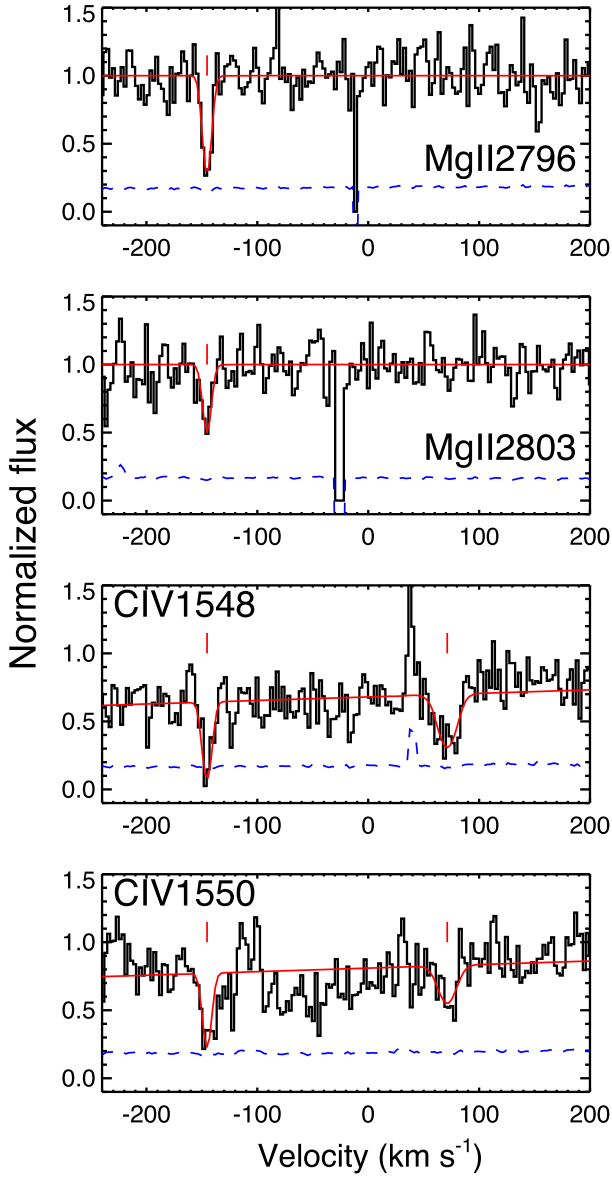


Figure B1. Keck/HIRES spectrum of the quasar close to the metal absorption lines of the system at $z \sim 1.104$. The zero velocity is set at $z = 1.10497$ that is the redshift of the closest galaxy to the sightline at $b = 243$ kpc. The C IV absorption profiles fall over the wing of a DLA at $z \sim 1.68$, where we have to modify the continuum by adding a line. The velocity of the absorbing components are indicated by tick marks. The blue dashed-lines present the error spectra.

Voigt profile consists of four components spread over 250 km s^{-1} . Fig. B4 shows the Keck/HIRES spectrum of this C IV absorbing system.

APPENDIX C: HOST GALAXY ABSORBERS

In this section we present a summary of host galaxy absorbers at $1.0 < z < 1.5$ towards the sightline of Q0152–020. We have only detected [O II] emission lines from the host galaxies in the cases of the systems at $z = 1.104$ and $z = 1.211$. With no other detections, we do not have the information required to correct the [O II] fluxes for internal dust attenuation. Since we do not detect the host galaxy absorbers associated with absorbing systems at $z = 1.224$ and $z =$

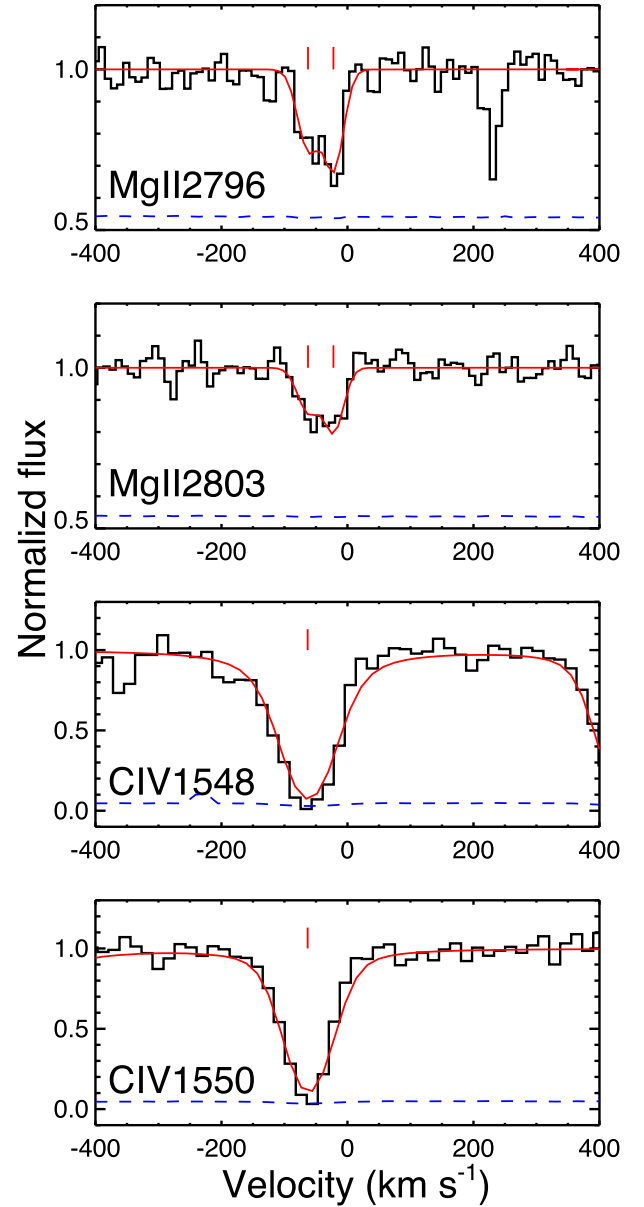


Figure B2. VLT/XShooter spectrum of the quasar close to the metal absorption lines of the system at $z \sim 1.211$. The zero velocity is set at $z = 1.21134$ that is the redshift of the closest galaxy to the sightline at $b = 40$ kpc.

1.480, we report the upper limits for their [O II] fluxes. Table C1 summarizes the extracted properties of these host galaxy absorbers. We have used the calibration of Kewley et al. (2004) to convert the [O II] flux to the SFR.

C1 Host galaxy absorbers at $z \sim 1.104$

We detected two [O II] emitters with redshifts close to the absorption redshift. The two galaxies are at large impact parameters of 243 kpc and 261 kpc. Fig. C1 presents the [O II] emission profile from these two emitters. As Fig. C1 shows, continuum emission is not detected from either of these two galaxies.

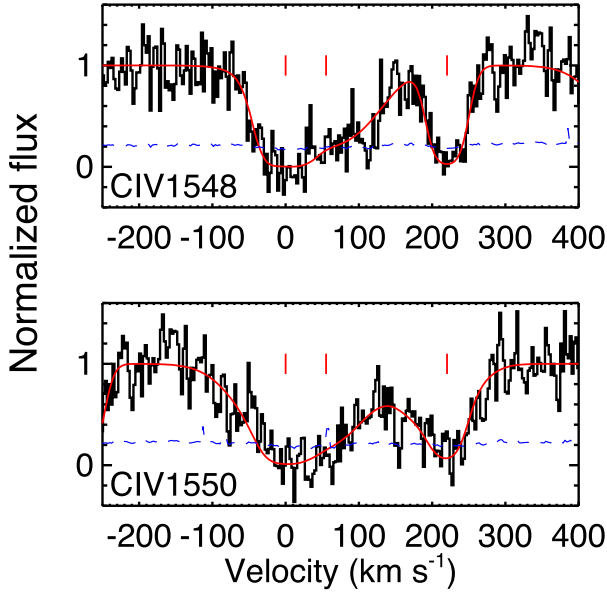


Figure B3. Keck/HIRES spectrum of the quasar close to C IV absorption profiles of the system at $z \sim 1.224$. The zero velocity is set at $z = 1.22430$. We have not detected any host galaxy close to the redshift of this absorbing system in our MUSE observation.

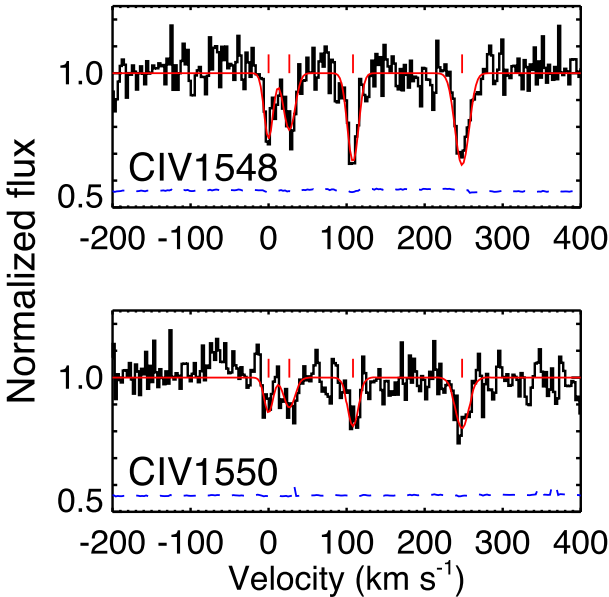


Figure B4. Keck/HIRES spectrum of the quasar close to C IV absorption profiles of the system at $z \sim 1.481$. The zero velocity is set at $z = 1.47981$. We have not detected any host galaxy close to the redshift of this absorbing system in our MUSE observation.

C2 Host galaxy absorbers at $z \sim 1.211$

Three [O II] emitters reside close to the absorption redshifts at impact parameters of 40 kpc, 71 kpc, and 164 kpc. Fig. C2 presents the spectra of these galaxies. The galaxy at the largest impact parameter has the strongest emission line and is also detected in the continuum. Inspecting the *HST*/WFPC2 images of these galaxies we note all the three emitters present perturbed morphologies which can be

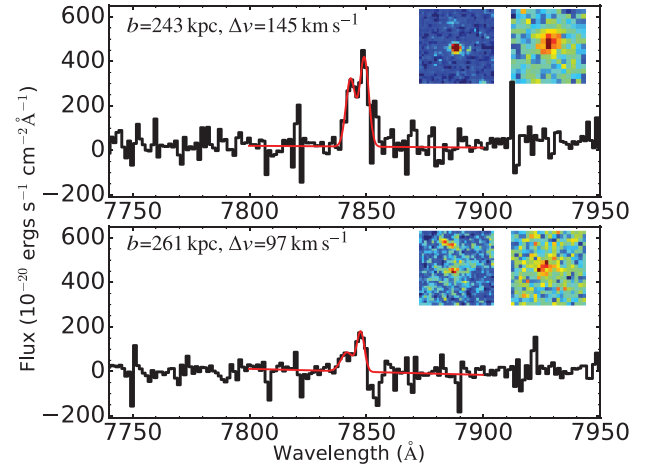


Figure C1. Spectra of the two [O II] emitters at $z = 1.104$. *HST* broad-band and MUSE [O II] narrow-band images of the emitters each with a size of $3'' \times 3''$ are presented on top right in each panel. The histogram and red curves in each panel present the observed and double-Gaussian-fitted to the [O II] emission, respectively. On the *top-left* side of each panel, we present the impact parameter and the velocity separation of the galaxy with respect to the absorber.

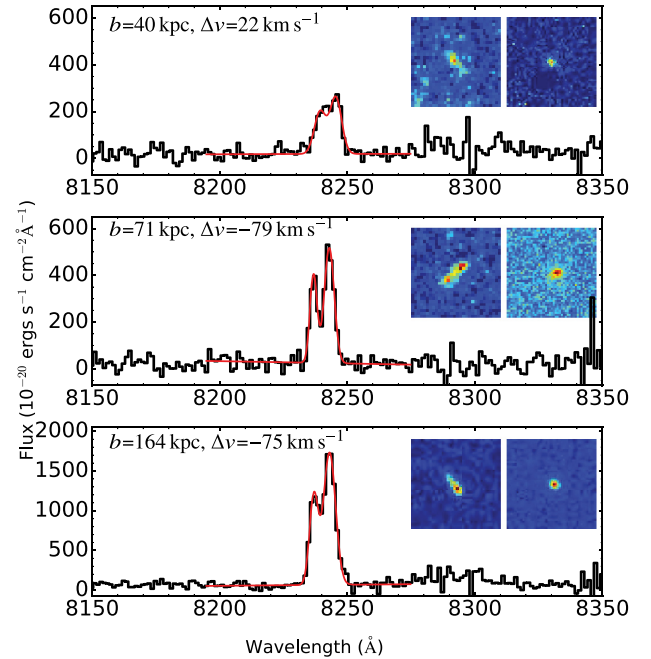


Figure C2. Same as Fig. C1 but for the system at $z = 1.211$.

signatures of recent interactions. In particular, for the case of the galaxy at $b = 71$ kpc, as presented in the middle panel of Fig. C2, we detect signatures of two cores at a distance of $\sim 0.6''$ ($\equiv 5$ kpc).

C3 Host galaxy absorbers at $z \sim 1.224$ and $z \sim 1.480$

We do not detect the host galaxies associated with the two C IV systems at $z_{\text{abs}} = 1.224$ and $z_{\text{abs}} = 1.480$. Hence, we estimate the 3σ upper limits for the fluxes of the [O II] emission lines and convert them to the upper limits on the SFR of the possible host galaxies.

Table C1. Extracted properties of host galaxy absorbers at $z > 1$.

z_{abs}	$\log N(\text{H I})$	$\log N(\text{Mg II})$	$\log N(\text{C IV})$	ID	RA (J2000)	Dec (J2000)	Redshift	b	Δv^1 10^{-17}	$f([\text{O II}])^2$	SFR ²
	[cm^{-2}]	[cm^{-2}]	[cm^{-2}]		hh:mm:ss	dd:mm:ss		[kpc]	[km s^{-1}]	[$\text{erg s}^{-1} \text{cm}^{-2}$]	[$M_{\odot} \text{yr}^{-1}$]
1.104	<16.8	12.48 ± 0.08	13.74 ± 0.09	G5	01:52:26.3	-20:01:33	1.10497 ± 0.00005	243	+150	3.4 ± 0.3	1.5 ± 0.4
				G6	01:52:29.1	-20:01:29	1.10463 ± 0.00006	261	+100	1.5 ± 0.2	0.7 ± 0.2
1.211	<16.6	12.93 ± 0.10	14.80 ± 0.10	G1	01:52:27.1	-20:01:02	1.21134 ± 0.00009	40	+20	2.4 ± 0.3	1.4 ± 0.4
				G3	01:52:27.5	-20:00:59	1.21059 ± 0.00002	71	-80	3.7 ± 0.1	2.1 ± 0.5
				G4	01:52:25.9	-20:01:01	1.21062 ± 0.00002	164	-80	14.6 ± 0.4	8.4 ± 2.1
1.224	<15.5	<11.8	14.92 ± 0.10	—	—	—	—	—	—	<0.4	<0.3
1.480	<16.0	<11.9	13.49 ± 0.02	—	—	—	—	—	—	<0.3	<0.3

Notes.

¹The velocity between the galaxy and the Mg II absorption component that has the highest $N(\text{Mg II})$.

²Estimated fluxes; hence the extracted SFRs have not been corrected for dust attenuation in the host galaxies.

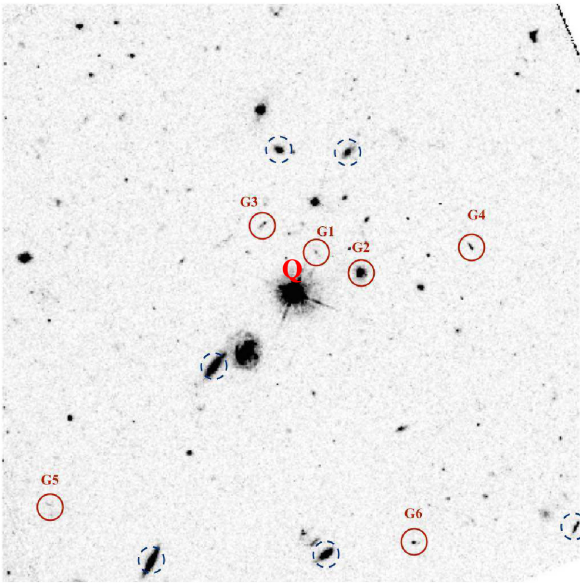


Figure C3. The $1' \times 1'$ *HST* WFPC2 *F720* image of the field of Q0152–020. The ‘G1’ to ‘G6’ letters mark the sky positions of the galaxies studied in this paper, ordered by impact parameter (see Table C1). ‘G2’ is associated with the absorber at $z_{\text{abs}} = 0.780$. The quasar resides in the centre of the field as indicated by Q. Dashed circles show the positions of galaxies with redshifts close to that of an LLS at $z = 0.38$ studied in Rahmani et al. (2018).

Table C1 presents the flux measurements for different absorbing galaxies. It is worth noting that in the two cases where we do not detect host galaxy absorbers we have not also detected signatures of cold gas (e.g., Mg II or Fe II lines) to be associated with the absorber. This may imply that such absorbers are produced at impact parameters larger than 250 kpc that is covered by MUSE or are associated with non-star-forming galaxies (e.g. Borthakur et al. 2013; Bordoloi et al. 2014b).

This paper has been typeset from a \LaTeX file prepared by the author.